Atomic-scale deformation mechanisms at high-pressure in hydroboracite, $CaMg[B_3O_4(OH)_3]_2 \cdot 3H_2O$

Davide Comboni[1*], Paolo Lotti[1], Lisa Chiappella[1], Tommaso Battiston[2], Gaston Garbarino[3], Paola Giura[4], G. Diego Gatta[1]

[1] Dipartimento di Scienze della Terra, Università degli Studi di Milano, Via Botticelli 23, 20133 Milano, Italy

[2] ZAG - Slovenian National Building and Civil Engineering Institute, Dimičeva ulica 12, 1000 Ljubljana, Slovenia

[3] ESRF – European Synchrotron Radiation Facility, 71 Avenue des Martyrs, CS 40220, 38043 Grenoble Cedex 9, France

[4]Sorbonne Université, Museum National d'Histoire Naturelle, UMR CNRS 7590, Institut de minéralogie, de physique des matériaux et de cosmochimie (IMPMC), 4 place Jussieu, F-75005 Paris, France

* **Corresponding Author:** Davide Comboni, davide.comboni@unimi.it

Davide Comboni: https://orcid.org/0000-0001-6445-3736

Paolo Lotti: https://orcid.org/ 0000-0003-2272-8281

Lisa Chiappella: https://orcid.org/0009-0007-6694-9904

Tommaso Battiston: https://orcid.org/0000-0003-1191-1363

Gaston Garbarino: https://orcid.org/0000-0003-4780-9520

Paola Giura: https://orcid.org/0000-0002-8489-0068

G. Diego Gatta: https://orcid.org/0000-0001-8348-7181

Abstract

The high-pressure behaviour of hydroboracite [ideally $CaMg[B_3O_4(OH)_3]_2 \cdot 3H_2O$, Sp. Gr. $P2/c$ with $a \sim 11.769$, $b \sim 6.684$, $c \sim 8.235$ Å, and $\beta \sim 102.6°$ at room conditions] has been studied by two *in-situ* single-crystal synchrotron X-ray diffraction experiments up to about 15 GPa, using He as pressure-transmitting medium. Between 14.51(5) and 14.72(5) GPa, hydroboracite undergoes a first-order phase transition to its high-pressure polymorph, hydroboracite-II (likely monoclinic with $a \sim 11.29$, $b \sim 6.297$, $c \sim 7.48$ Å, and $\beta \sim 106°$, space group unknown). The isothermal bulk modulus ($K_{V0} = \beta^{-1}_{P0,T0}$, where $\beta_{P0,T0}$ is the volume compressibility coefficient) of hydroboracite was found to be $K_{V0} = 41.4(6)$ GPa. The destructive nature of the phase transition prevented any structure resolution of hydroboracite-II or even the continuation of the experiments at pressures higher than 15.45(5) GPa. In the pressure range 0-14.45(5) GPa, the compressional anisotropy of hydroboracite, indicated by the ratio between the principal components of the unit-strain ellipsoid, is $\varepsilon_1:\varepsilon_2:\varepsilon_3 = 2.2:1.3:1$. The *P*-induced deformation mechanisms at the atomic scale in hydroboracite are here described.

Keywords: hydroboracite, high-pressure, single crystal X-ray diffraction, elastic compressibility, phase transition

1. Introduction

Borates are classified as critical raw materials by the European Union (Blengini et al. 2020), as they constitute the primary source of boron, an element used in a variety of different industrial sectors (*e.g.*, Ezechi et al. 2011; Huang et al. 2020; Waleed KH. Sh. Al-Juheishy 2020). Hydroboracite, with the ideal chemical formula $CaMg[B_3O_4(OH)_3]_2 \cdot 3H_2O$, is a hydrous borate of calcium and magnesium that naturally forms in evaporitic borate environments. Typically, hydroboracite occurs alongside minerals such as colemanite, inyoite, and ulexite, and can also originate from the alteration of colemanite in groundwater systems (Helvaci 2017; Demircioglu 2023). The mineral was first described in 1834 in the Atyrau Province of present-day Kazakhstan. Later occurrences were reported in the salt deposits of the Stassfurt basin (Germany), in Ryan (California)—where it was found in association with colemanite and calcite—and near the Inder Lake in western Kazakhstan (formerly U.S.S.R.), where economically viable deposits were discovered alongside colemanite, inyoite, ulexite, and inderite (Foshag 1924; Fischer and Lischke 1981; Pekov and Abramov 1993). Currently, the most economically important hydroboracite occurrences are documented in the Bigadiç boron district, where the mineral appears in nodular form—ranging from 5 to over 30 cm in size—typically associated with ulexite, colemanite, and inyoite (Demircioglu 2023). Hydroboracite continues to attract scientific interest due to both its geological significance and its structural complexity (Ashirov et al. 1962; Frost et al. 2014). From a crystallographic perspective, hydroboracite crystallizes in the monoclinic system (space group *P*2/*c*), and its structure is built around the $[B_3O_4(OH)_3]^{2-}$ anionic group (Sabelli et al. 1978). This unit consists of two $B\varphi_4$ tetrahedra and one BO_3 triangle, interconnected at their corners to form undulating polymeric chains extending along the *c*-axis (Figure

1). These borate chains are incorporated into a layered framework through their connection with $Mg(H_2O)_4(OH)_2$ octahedra—linked via corners and forming chains parallel to *c*, similarly to colemanite (Christ et al. 1954), —and with edge-sharing $Ca\varphi_8$ polyhedra (where φ denotes H_2O, OH^-, or O atoms) (Fig. 1). These features collectively contribute to build a robust three-dimensional structural network (Sabelli et al. 1978). Recent spectroscopic investigations have provided insights into the bonding and structural dynamics of hydroboracite. In particular, Raman and infrared (IR) spectroscopies have proven valuable in identifying the vibrational modes associated with both the borate groups and the H_2O/hydroxyl units (Frost et al. 2014).

Due to their relatively high thermal neutron absorption cross-section (~3840 barns for ^{10}B, which comprises ~20% of natural boron (Carter et al. 1953; Palmer and Swihart 1996)) and their low production cost, hydrous borates are considered as promising components for use in neutron-shielding concretes (Okuno 2005; Okuno et al. 2009; Glinicki et al. 2018). Given its low density (2.17 g/cm^3) and high B_2O_3 content (~50 wt%), hydroboracite is a suitable candidate for such applications. Although it is not among the most abundant hydrated borates in nature, it frequently occurs in association with colemanite and ulexite in major borate deposits, such as those at Bigadiç and Emet (Turkey) (Helvaci and Alonso 2000). As such, beyond its mineralogical interest, hydroboracite holds potential as a boron-rich precursor for the production of functional shielding materials. Since 2019, several studies have focused on the behaviour of hydrous borates under non-ambient conditions (*e.g.*, Lotti et al. 2018; Comboni et al. 2020a, 2022b, 2023, 2024; Pagliaro et al. 2021) with the aim of assessing their stability at extreme conditions. For these reasons, we investigated the high-pressure behaviour of hydroboracite by means of *in situ* single-crystal X-ray diffraction under hydrostatic conditions in order to: *i*) track the compressional path, based on the experimental *P–V* data, *ii*) derive the elastic parameters using an isothermal equation-of-state formalism, (*i.e.,* axial and volumetric bulk moduli), currently unavailable in the literature; *iii*) investigate the phase-stability field of hydroboracite at high pressure, and compare it with other hydrated borates (*e.g.*, colemanite, kernite); *iv*) describe the high-pressure structural re-arrangement of hydroboracite at the atomic scale. This work is part of a long-term project devoted to investigate the crystal chemistry and the *PT* stability of a variety of hydrated borate minerals, as potential aggregates in neutron shielding concretes.

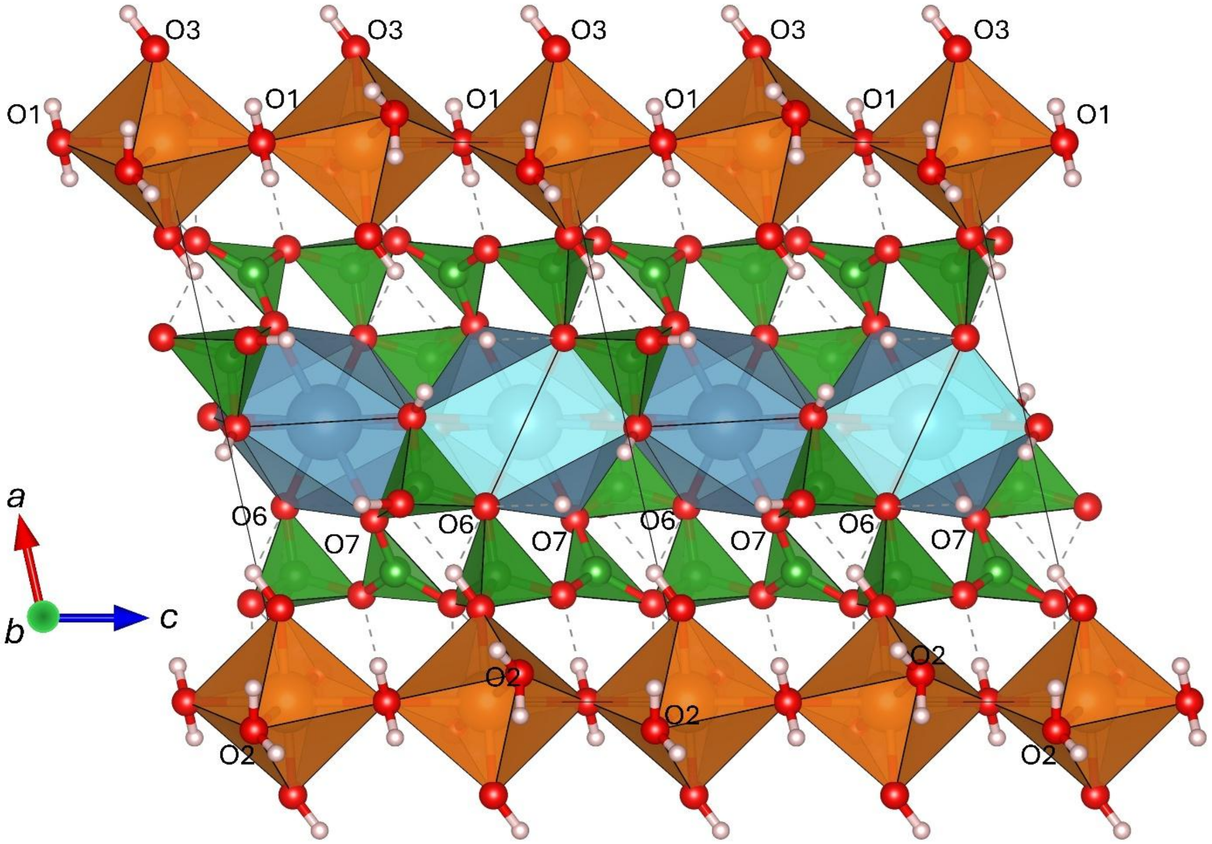

Figure 1: Hydroboracite structure, based on the model proposed by Sabelli et al. (1978), viewed down the [010] direction. Ca-polyhedra in *indigo*, Mg- polyhedra in *orange*, boron polyhedra in *green*.

2. Experimental procedures

Hydroboracite is a light (2.17 g/cm^3) and soft (2.5 on the Mohs scale) mineral, typically exhibiting a prismatic habit. The hydroboracite sample used in this study was sourced from the Bigadiç Mine, Turkey, and provided by the Sorbonne Université, Muséum National d'Histoire Naturelle, Paris (France), in the form of a few microcrystals. The paucity of the sample did not allow a full chemical characterization; however, the unit-cell parameters were consistent with a crystal with ideal composition (as reported in previous studies), and the structure refinement (described below) proved non-significant substitutions for the main chemical component (*i.e.*, B, Ca, Mg and O). Two single crystals, each measuring approximately 20x5x4 μm^3, were selected for high-pressure experiments at the ID15b beamline, ESRF, Grenoble (France). The diffraction experiment employed a convergent monochromatic beam (E~30 keV, λ~0.41 Å and ~200 mA). Helium was used as the pressure-transmitting medium (Klotz et al. 2009), and two ruby microspheres were added as pressure calibrants (pressure uncertainty ± 0.05 GPa; Mao et al. 1986). The crystals were loaded into two different membrane-driven DACs (diamond anvil cells), with 600 μm culet Boehler-Almax design anvils. For each DAC, a stainless-steel foil (with thickness~250 μm) was pre-indented to about 80 μm and then drilled by spark-erosion, leading to a pressure chamber of ~300 μm in diameter. The diffraction patterns were collected by an Eiger2X 9M detector, positioned about 180 mm from the sample. The sample-to-detector distance was calibrated using a Si standard and a vanadinite ($Pb_5(VO_4)_3Cl$) single crystal. A pure ω-scan ($-32° \leq \omega \leq +32°$) was used to collect the diffraction patterns, with a 0.5° step width and a 0.5 s exposure time per step. Additional technical details regarding the beamline setup are available in (Hanfland 2016; Poreba et al. 2022).

3. Data analysis

The CrysAlisPro software suite (Rigaku Oxford Diffraction 2019) was used to index the diffraction peaks and integrate their intensities; Lorentz-polarization corrections were also applied. To compensate for X-ray absorption due to the DAC components, the semi-empirical ABSPACK routine, implemented in CrysAlisPro, was employed. Table 1 lists the unit-cell parameters at high pressure, and their evolution with P is shown in Figure 2. Selected diffraction patterns are shown in Figure 3. All structure refinements were carried out using the JANA2006 software (Petrícek et al. 2014), starting from the initial fractional coordinates reported by Sabelli, Stoppioni, and Lamarmora (Sabelli et al. 1978), and without the H atoms (as not refinable at high pressure). CIFs (crystallographic information files) are deposited as Supplementary Materials. High-pressure data were collected up to 15.45(5) GPa, as the number and intensity of the observed reflections (*i.e.,* with $F_o^2 > 3\sigma(F_o^2)$) significantly decreased after the phase transition at 14.51(5) GPa (as Figure 3 shows), effectively ending the experiments. In both the experiments, crystals did not recover after the phase transition. A similar "destructive" phase transition was observed in inderborite (Comboni et al. 2024); similarly, the modest number of reflections collected after the transition was barely sufficient to index the unit cell of the high-pressure polymorph, hydroboracite-II, which was found to be metrically monoclinic. However, the space group remains a matter of discussion due to the large uncertainties in the unit-cell parameters, and it cannot be ruled out the possibility that hydroboracite-II is not monoclinc, but rather triclinic. Relevant interatomic distances, average bond lengths, angles, polyhedral volumes, and structural distortion parameters were calculated using tools integrated in the VESTA software (Momma and Izumi 2008). The distortion parameters include:

i) the **distortion index** $D = \frac{1}{n}\sum_{i=1}^{n}\frac{|l_i - l_{av}|}{l_{av}}$, where l_i is the distance from the central atom to the i^{th} coordinating atom, and $l_{av}$is the average bond length (Baur 1974);

ii) **the quadratic elongation** $<\lambda>= \frac{1}{n}\sum_{i=1}^{n}\left(\frac{l_i}{l_0}\right)^2$, where l_0 is the center-to-vertex distance of a regular polyhedron of the same volume and l_i is the actual center-to-vertex length (Robinson et al. 1971) and

iii) **the bond angle variance** as $\sigma^2 = \frac{1}{m-1}\sum_{i=1}^{m}(\phi_i - \phi_0)^2$ where *m* is the number of faces in the polyhedron×3/2, *i.e.*, number of bond angles, ϕ_i is the i^{th} bond angle, and ϕ_0 is the ideal bond angle for a regular polyhedron *e.g.,* 90°for an octahedron (Robinson et al. 1971).

The calculated parameters are listed in Tables S1 and S2 for the first and second datasets, respectively. Relevant interatomic angles are reported in Table S2.

The (isothermal) compressional behaviour of hydroboracite was described using a III- and II-order Birch–Murnaghan Equations of State (Birch 1947), respectively, for the unit cell of hydroboracite and for its $Ca\varphi_8$ and $Mg\varphi_6$ polyhedra (Table 2). This equation of state (EoS) allows to refine the bulk modulus (K_{V0} or $K_{P0,T0}$, defined as $-V_0(\partial P/\partial V)_{T0} = \beta^{-1}_{P0,T0}$, where $\beta_{P0,T0}$ is the volume compressibility coefficient at room conditions) and its *P*-derivatives ($K' = \partial K_{P0,T0}/\partial P$ and $K'' = \partial^2 K_{P0,T0}/\partial P^2$). Expansion in the Eulerian strain polynomial has the following form:

$$P(fe) = 3K_{P0,T0}\, fe\, (1 + 2fe)^{5/2}\ \{1 + 3/2(K' - 4)fe + 3/2[K_{P0,T0}K'' + (K' - 4)(K' - 3) + 35/9]fe^2 + ...\}.$$

When truncated to the second order in energy, *i.e.* with $K' = \partial K_{P0,T0}/\partial P = 4$, the EoS reduces to:

$$P(fe) = 3K_{P0,T0}\, fe(1 + 2fe)^{5/2}.$$

The truncation to the second order in energy is reasonable when the experimental data plot follows a horizontal trend in the diagram with Eulerian strain ($fe = \frac{1}{2}\left[(V_0/V)^{2/3} - 1\right]$) *vs*. normalised pressure (F, defined as $F = P/\left[3fe(1 + 2fe)^{5/2}\right]$). The BM-EoS parameters (listed in Table 2) were refined by minimizing the differences between the EoS curves and the experimental data, which were weighted by their uncertainties in P and V. The third-order BM EoS was used to fit the unit-cell parameters of hydroboracite, whereas the PV data pertaining to the Ca, Mg and B polyhedral volumes were modelled with a II-BMS. The fitting was carried out using the EOS-FIT7-GUI software (Angel et al. 2014; Gonzalez-Platas et al. 2016). An estimated uncertainty of ± 0.05 GPa was considered for pressure (Mao et al. 1986) during the data fitting. The *fe-F* plot is shown in Figure S1.

Figure 2: Evolution of the normalized unit-cell parameters and unit-cell volume of hydroboracite with pressure; data pertaining to the first and the second datasets are in *blue* circles and red diamonds, respectively (empty markers represent the high-pressure polymorph). Refined III-order BM EoS has been drawn as dashed lines.

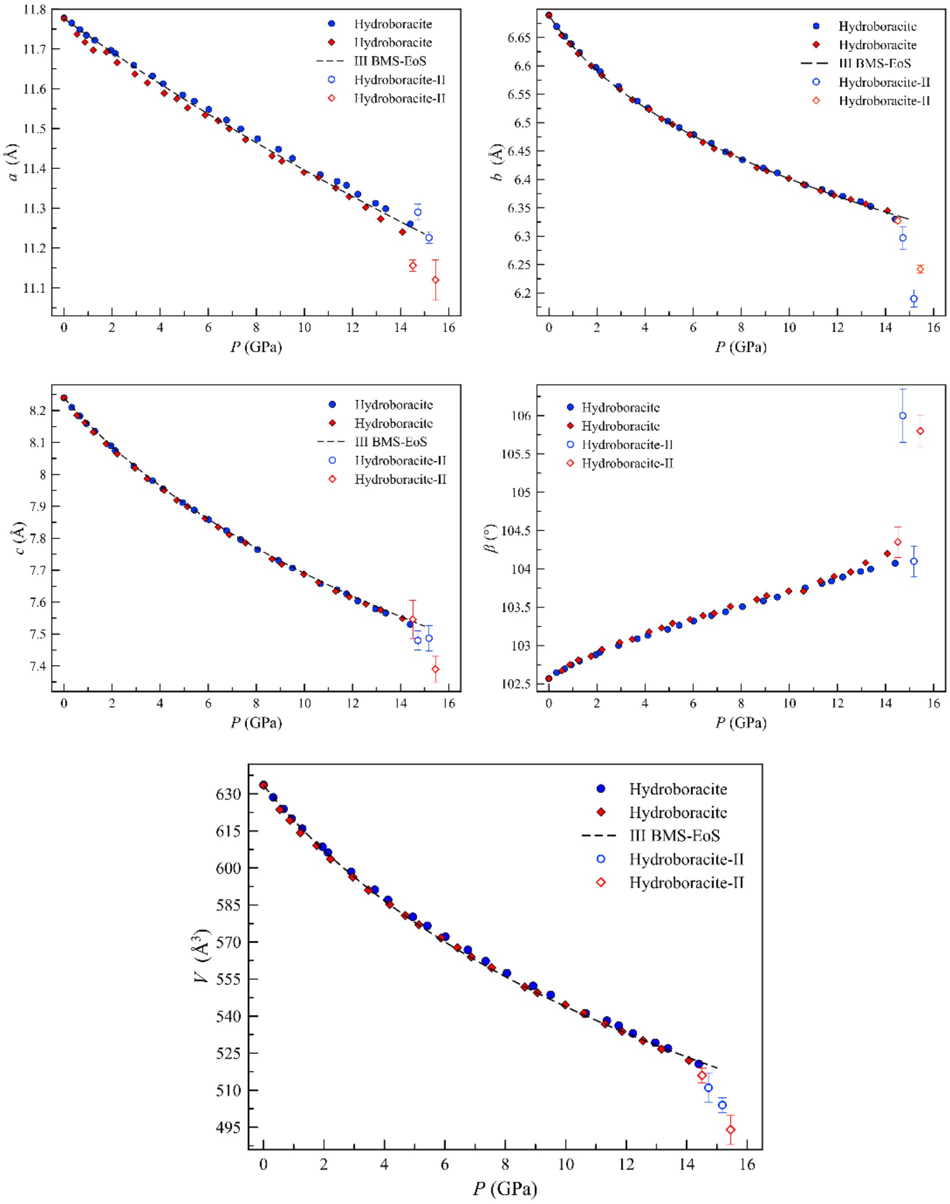

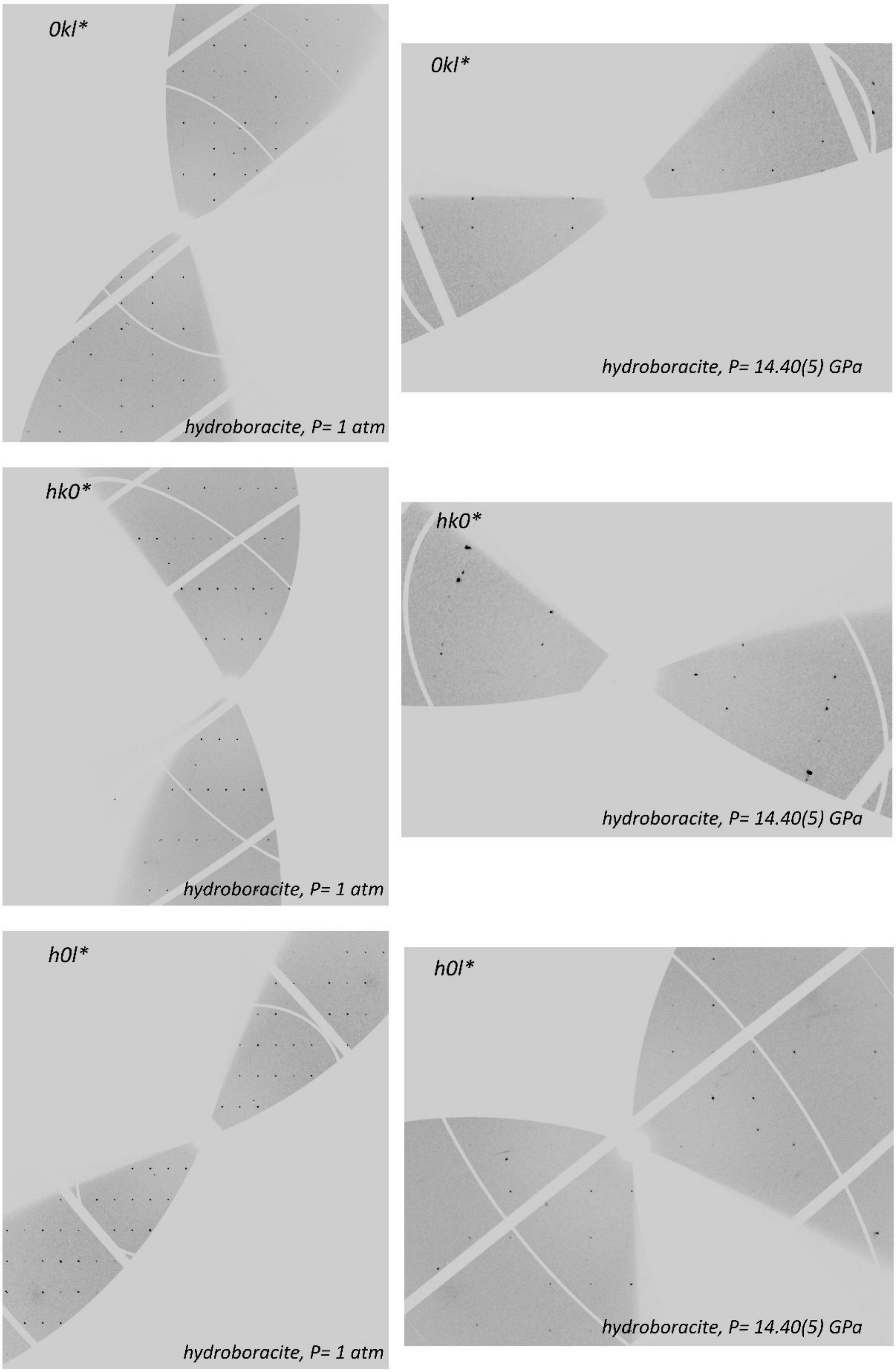

Figure 3: Reconstruction, based on the experimental XRD data, of the *0kl*, hk0* and h0l** reciprocal lattice planes of hydroboracite at ambient pressure (*left side*) and at 14.40(5) GPa (*i.e.,* just below the phase transition pressure) (*right side*). After the phase transition, the number of observed reflections dropped dramatically.

Table 1 Evolution of the unit-cell parameters of hydroboracite with pressure refined from the two independent experiments (*high-pressure polymorph). **-First datatset-**

P(GPa)	**a(Å)**	**b(Å)**	**c(Å)**	**β(°)**	**V(Å^3)**
0.0001	11.7780(2)	6.68952(7)	8.2398(1)	102.569(2)	633.65(2)
0.32(5)	11.7651(5)	6.6695(6)	8.2102(2)	102.646(2)	628.60(7)
0.66(5)	11.7489(6)	6.6520(7)	8.1829(2)	102.695(2)	623.89(7)
0.93(5)	11.7345(5)	6.6387(6)	8.1593(2)	102.746(2)	619.95(6)
1.28(5)	11.7221(7)	6.6236(9)	8.1349(2)	102.798(3)	615.92(9)
1.95(5)	11.6966(5)	6.5978(6)	8.0899(2)	102.879(2)	608.61(7)
2.13(5)	11.6891(5)	6.5903(6)	8.0748(2)	102.914(2)	606.30(6)
2.90(5)	11.6593(7)	6.5641(8)	8.0254(2)	103.001(3)	598.46(9)
3.68(5)	11.6322(6)	6.5381(7)	7.9804(2)	103.087(3)	591.17(7)
4.12(5)	11.6127(6)	6.5260(7)	7.9545(2)	103.133(3)	587.06(7)
4.94(5)	11.5844(7)	6.5028(8)	7.9117(2)	103.211(3)	580.22(8)
5.42(5)	11.5689(6)	6.4914(7)	7.8882(2)	103.264(3)	576.59(7)
6.02(5)	11.5481(5)	6.4791(6)	7.8585(2)	103.320(2)	572.16(6)
6.76(5)	11.5215(6)	6.4637(7)	7.8243(2)	103.392(3)	566.84(7)
7.35(5)	11.4991(5)	6.4486(6)	7.7959(2)	103.440(2)	562.26(6)
8.05(5)	11.4744(5)	6.4347(7)	7.7645(2)	103.508(2)	557.42(6)
8.92(5)	11.4480(5)	6.4200(7)	7.7306(2)	103.582(2)	552.27(6)
9.50(5)	11.4251(6)	6.4116(7)	7.7067(2)	103.633(3)	548.63(7)
10.66(5)	11.3844(5)	6.3901(6)	7.6577(2)	103.752(2)	541.11(6)
11.36(5)	11.3673(5)	6.3824(7)	7.6388(2)	103.809(3)	538.18(7)
11.75(5)	11.3575(6)	6.3755(7)	7.6259(2)	103.840(3)	536.16(6)
12.22(5)	11.3350(5)	6.3705(7)	7.6038(2)	103.894(2)	533.00(6)
12.99(5)	11.3123(9)	6.361(1)	7.5788(3)	103.967(5)	529.2(1)
13.38(5)	11.2986(5)	6.3526(8)	7.5660(2)	103.998(3)	526.92(7)
14.40(5)	11.2604(7)	6.330(1)	7.5304(2)	104.074(4)	520.65(9)
14.72(5)*	11.29(2)	6.30(2)	7.48(3)	106.0(4)	511(6)
15.18(5)*	11.23(2)	6.19(2)	7.49(4)	104.1(2)	504(3)

-Second dataset-					
P(GPa)	**a(Å)**	**b(Å)**	**c(Å)**	**β(°)**	**V(Å^3)**
0.0001	11.7763(2)	6.68881(7)	8.2394(1)	102.567(2)	633.46(1)
0.54(5)	11.734(9)	6.6535(4)	8.1866(7)	102.68(3)	623.6(5)
0.87(5)	11.717(5)	6.6391(1)	8.1621(4)	102.75(2)	619.3(3)
1.22(5)	11.697(5)	6.6216(1)	8.1323(4)	102.81(2)	614.2(3)
1.76(5)	11.692(5)	6.6002(2)	8.0961(4)	102.86(2)	609.1(3)
2.21(5)	11.666(5)	6.5832(2)	8.0646(4)	102.95(2)	603.6(3)
2.95(5)	11.637(5)	6.5587(2)	8.0198(4)	103.04(2)	596.3(2)
3.47(5)	11.615(5)	6.5404(2)	7.9867(4)	103.08(2)	591.0(2)
4.17(5)	11.589(5)	6.5230(2)	7.9506(4)	103.18(2)	585.2(3)
4.69(5)	11.575(4)	6.5067(1)	7.9195(4)	103.23(2)	580.7(2)
5.14(5)	11.552(5)	6.4969(2)	7.8989(5)	103.29(2)	577.0(3)
5.87(5)	11.534(6)	6.4789(2)	7.8618(5)	103.34(2)	571.7(3)
6.41(5)	11.520(5)	6.4655(1)	7.8351(4)	103.39(2)	567.7(2)
6.87(5)	11.500(4)	6.4542(1)	7.8111(3)	103.42(2)	563.9(2)
7.55(5)	11.472(6)	6.4444(2)	7.7853(5)	103.51(2)	559.6(3)
8.65(5)	11.431(5)	6.4208(2)	7.7347(5)	103.60(2)	551.8(3)
9.06(5)	11.418(5)	6.4152(2)	7.7187(4)	103.65(2)	549.4(2)
9.98(5)	11.390(4)	6.4017(1)	7.6875(4)	103.71(2)	544.5(2)
10.59(5)	11.377(5)	6.3909(1)	7.6620(4)	103.71(2)	541.1(2)
11.30(5)	11.351(5)	6.3801(2)	7.6347(5)	103.84(2)	536.8(3)
11.86(5)	11.329(4)	6.3721(1)	7.6167(3)	103.90(2)	533.8(2)
12.55(5)	11.302(4)	6.3645(1)	7.5941(4)	103.96(2)	530.1(2)
13.17(5)	11.273(5)	6.3567(2)	7.5760(5)	104.08(2)	526.6(3)
14.08(5)	11.244(12)	6.3448(5)	7.549(1)	104.20(5)	522.1(5)
14.51(5)*	11.16(1)	6.327(5)	7.55(6)	104.4(2)	516(3)
15.45(5)*	11.12(5)	6.242(7)	7.39(4)	105.8(2)	494(6)

Table 2: Refined elastic parameters pertaining to hydroboracite, based on the isothermal third-order BM Equation of State fits, and elastic parameters pertaining to the Ca, Mg- and B-coordination polyhedra of hydroboracite, based on the isothermal second-order BM Equation of State fits (*fixed parameter).

	V_0, x_0 (Å^3, Å)	**$K_{V0,x0}$ (GPa)**	**K'**	**$\beta_{V0,x0}$ (GPa^{-1})**
V	633.46(2)	41.4(6)	6.1(2)	0.0242(4)
a	11.7763(1)	90(2)	2.5(4)	0.0037(1)
b	6.6876(2)	34(1)	14(1)	0.0098(3)
c	8.2396(1)	31.9(2)	3.88(5)	0.0104(1)
CaO_8	24.79(6)	74(3)	4*	0.0135(5)
MgO_6	12.20(3)	87(3)	4*	0.0115(4)
$B1O_4$	1.648(3)	236(15)	4*	0.0043(3)
$B2O_4$	1.647(3)	254(17)	4*	0.0039(3)

4.0 Results

4.1 Elastic behaviour

Referring to the first dataset (Table 1), between ambient pressure and 14.40(5) GPa, the length of the unit-cell edges of hydroboracite decreases steadily by about 4.4% and 5.4% for the *a* and *b* edges and by about 8.6% along the *c* edge. The unit-cell volume decreases monotonically by about 17.8% and the β angle steadily increases by about 1.5% (see Table 1). Similar values (*i.e.,* within 3σ) were observed for the second dataset. Up to 14.40(5) GPa, the crystal structure of hydroboracite deforms steadily with no significant changes. Between 14.40(5) and 14.51(5) GPa, hydroboracite undergoes a phase transition to its high-pressure polymorph, hydroboracite-II. Unlike other phase transitions in hydrous borates (*e.g.*, jadarite, Comboni et al. 2022b, or colemanite, Lotti et al. 2017), which are characterized by a sharp volume collapse, in hydroboracite the unit-cell volume decreases only slightly. More in detail, in jadarite, ΔV is about 3%. In hydroboracite, if we compare the last point where hydroboracite-I is observed (*i.e.*, at 14.40(5) GPa, $V = 520.65(9)$ Å³) with the first point where hydroboracite-II appears (*i.e.*, 14.51(5) GPa, $V = 516(3)$ Å³), the volume difference is only 0.9(6)%. This difference is also clearly visible in Fig. 2. However, the phase transition is highly disruptive: data could only be collected up to 15.45(5) GPa, as the number and intensity of the observed reflections (*i.e.*, with $F_o^2 > 3\sigma(F_o^2)$) dropped significantly above the phase transition (down to about 40 observed reflections). This is particularly noteworthy, because at pressures above ~16 GPa, the diffraction peaks became too sparse to allow reliable indexing. Upon decompression, the crystal structure of hydroboracite does not revert to its ambient-pressure polymorph, suggesting that the phase transition is irreversible.

As already indicated by the evolution of the unit-cell parameters and also by the linear elastic parameters, listed in Table 2, hydroboracite is an anisotropic mineral, particularly stiffer along the *a* crystallographic edge. However, in monoclinic crystals, the unit-cell angle β varies freely with pressure, meaning that the linear bulk moduli along the principal crystallographic directions (listed in Table 2) do not fully describe the compressional anisotropy. To overcome this problem, the Eulerian finite strain analysis was performed with the *Win_Strain* software (Angel 2011). The geometrical relationships between the unit-strain ellipsoid (calculated between ambient pressure and 14.40(5) GPa) and the crystallographic axes of hydroboracite can be described by the following matrix (with $\varepsilon_1 > \varepsilon_2 > \varepsilon_3$):

$$\begin{pmatrix} \varepsilon_1 \\ \varepsilon_2 \\ \varepsilon_3 \end{pmatrix} \angle \begin{pmatrix} 83(1)^\circ & 90^\circ & 21(1)^\circ \\ 90^\circ & 180^\circ & 90^\circ \\ 7(1)^\circ & 90^\circ & 111(1)^\circ \end{pmatrix} \cdot \begin{pmatrix} a \\ b \\ c \end{pmatrix}$$

The obtained parameters ($\varepsilon_1:\varepsilon_2:\varepsilon_3$ = 2.2:1.3:1, ε_1=0.00672(2) GPa^{-1}; ε_2=0.00383(2) GPa^{-1}; ε_3=0.00301(1) GPa^{-1}) highlight that the response of hydroboracite to compression is anisotropic with the principal compression direction (ε_1) forming an angle of 21° with the *c* edge. This elastic anisotropy is surprisingly modest if compared to other hydrous borates such as meyerhofferite ($\varepsilon_1:\varepsilon_2:\varepsilon_3$ = 5.8:4.7:1) or inyoite ($\varepsilon_1:\varepsilon_2:\varepsilon_3$= 3.5:2.1:1) (Comboni et al. 2020b, 2022a). Regarding the high-pressure polymorph, the poor quality of the diffraction data did not allow any robust calculation of the elastic parameters.

4.2 Structure evolution

The high-quality structure refinements of hydroboracite enabled a detailed description of the main deformation mechanisms that accommodate compression between ambient pressure and 14.40(5) GPa. The bulk moduli (K_{V0}) of the $B\varphi_4$ tetrahedra, based on a second-order isothermal Birch-Murnaghan Equation of State fit (*i.e.,* 236(15) and 254(17) GPa, respectively for K_{VB1O4} and K_{VB2O4}**,** Table 2), is about six times larger than that of the hydroboracite unit-cell. This indicates that the boron tetrahedra behave as "quasi" uncompressible units, as expected at low to moderate pressures (Table 2). A similar response has been reported in all hydrated borates studied so far under compression (*e.g.,* ulexite, jadarite, kernite; Comboni et al. 2020a, 2021, 2022b) as well as in other anhydrous borates (*e.g.,* reedmergnerite, londonite, barium metaborates; Gatta et al. 2011; Bekker et al. 2022; Gorelova et al. 2022).

By contrast, the $Mg\varphi_6$ octahedra and $Ca\varphi_8$ polyhedra are significantly softer, similarly to what observed in inderborite (Comboni et al. 2024). However, in hydroboracite, the difference between the two is within 2σ (Table 2). Notably, the Ca polyhedron is significantly stiffer in hydroboracite ($K_{VCa\varphi8}$ = 74(3) GPa) than in other borate structures (like inderborite, inyoite and meyerhofferite, respectively 53(4), 54(8) and 55(10) GPa) (Comboni et al. 2020b, 2022a, 2024). Furthermore, both the $Mg\varphi_6$ and $Ca\varphi_8$ polyhedra deform progressively, but remain close to their original configurations, as evidenced by the distortion parameters reported in Tables S1 and S2. When compared with the bulk modulus of hydroboracite, all the polyhedra are substantially stiffer than the crystal structure as a whole (Table 2), implying that other mechanisms must accommodate the deformation induced by the applied pressure.

Indeed, tilting around the oxygen hinges linking the B-, Ca- and Mg- polyhedra can be deduced from the data in Table S1 and S2, which reports significant variations in the O–O–O angles and other interatomic distances with increasing pressure. Specifically, the O7– $\widehat{O6}$ –O7, Mg–$\widehat{O1}$–Mg and O2–$\widehat{O1}$–O2 angles, describing tilting within the $Mg\varphi_6$ and $Ca\varphi_8$ chains, decrease steadily by 8.9(3)°, 3.7(5)° and 5.1(3)°, respectively, between ambient pressure and 14.40(5) GPa (Figure 4). Another mechanism accommodating the pressure-induced deformations is the compression of the hydrogen-bonding network, whose evolution plays a role in the destabilization of the crystal structure.

For instance, the H_2O molecule of the O2 atom (which is in coordination with the $Mg\varphi_6$ octahedron) is connected, via hydrogen bonding, to O5, which belongs to the planar trigonal BO_3^{2-} group (Figure 4). At ambient pressure, the interatomic angle $O2–\widehat{O5}–O3$ is 120.9(1)°, and, as pressure increases to 14.40(5) GPa, it raises progressively to ~124.3(5)° (Table S1, S2). Likewise, also the $O1\cdots O4$ distance (where O1 belonging to a H_2O molecule is the hinge that connects the Mg polyhedra along the *c* axis and acts as a donor in two hydrogen bonds, and O4 is the oxygen hinge between the planar trigonal group BO_3 and the $B1\varphi_4$ tetrahedra and acceptor of one hydrogen bond) decreases steadily with pressure from 2.684(2) to 2.47(1)Å (notably 0.2 Å is about 10% of the initial distance). In the same *P*-range, a similar decrease in bond length was observed for $O2\cdots O5$ (from 2.715(3) to 2.594(6) Å). These observations highlight that the main mechanisms with which the structure deforms are (*i*) tilting around inter-polyhedral oxygen hinges and (*ii*) compression of the hydrogen bonding network. These mechanisms are analogous to what was observed in several other hydrous borate structures, characterized by a pervasive hydrogen bonding network, which plays a paramount role in the stability of the crystalline edifice (*e.g.*, meyerhofferite, inyoite, inderborite; Comboni et al. 2020b, 2022a, 2024). It is therefore likely that the combination of these two mechanisms underlies the relatively low bulk modulus of hydroboracite. Figure 5 shows the evolution of some selected geometrical parameters, normalized to ambient pressure values, showing nearly linear trends throughout the H*P*-ramps. This suggests that the progressive deformation of the crystal structure evolves monotonically up to the pressure at which hydroboracite undergoes its phase transition.

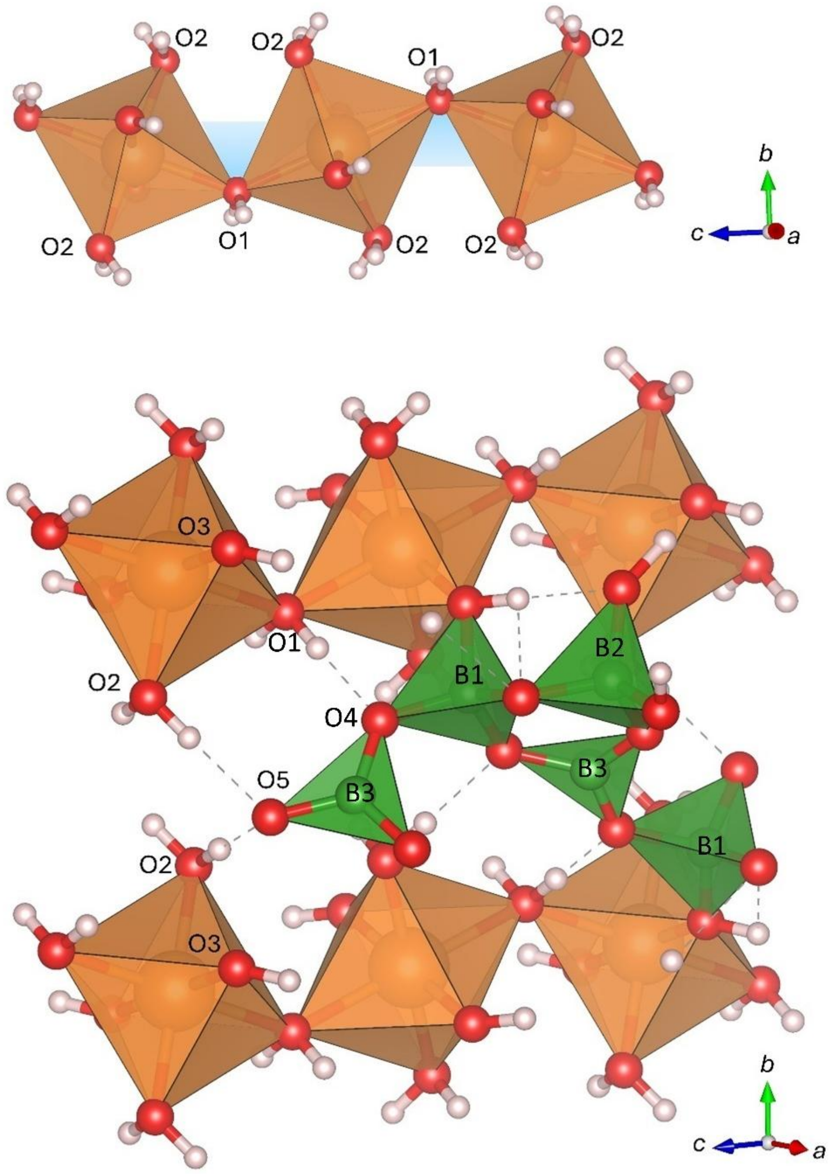

Figure 4: Clinographic views of the structure of hydroboracite by Sabelli et al. (1978) showing the Mg-chains (top) and the hydrogen-bonding network (bottom) at ambient pressure.

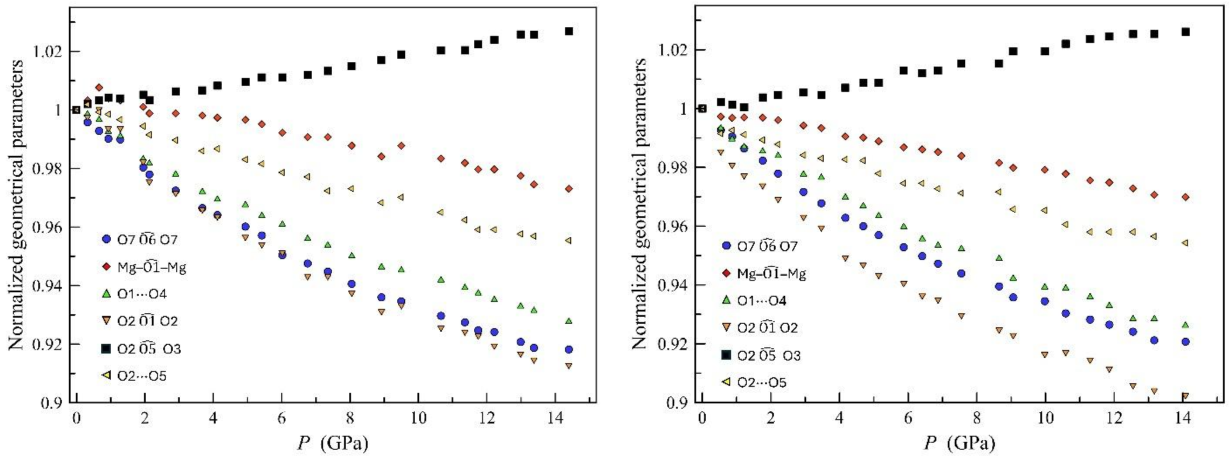

Figure 5: Evolution of some selected geometrical parameters, normalized to the values at ambient pressure (first dataset on the left, second dataset on the right). O7—$\widehat{O6}$—O7 in *blue circles*, Mg–$\widehat{O1}$–Mg in *red diamonds*, O1···O4 in *upwards green triangles*, O2–$\widehat{O1}$–O2 in *downwards orange triangles*, O2 $\widehat{O5}$ O3 in *black squares* and in O2···O5 *leftwards yellow triangles.*

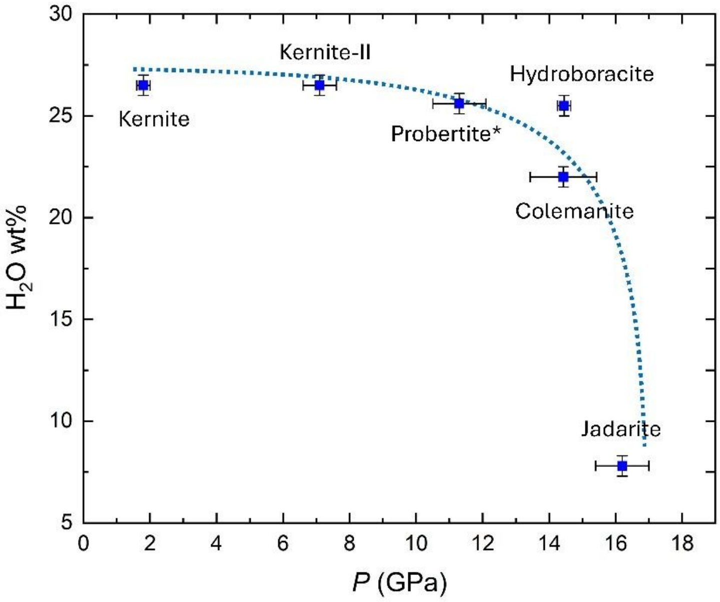

Figure 6: H_2O content *vs.* pressure at which phase transitions occur in borate structures characterized by endless $B\varphi_x$ units. A qualitative correlation is represented by the dotted sky-blue line.

5. Concluding remarks

In this study, we investigated the high-pressure behaviour, at room temperature, of hydroboracite through *in situ* single crystal X-ray diffraction up to ~15.5 GPa. Data collected at high-pressure revealed that:

(1) The ambient-condition polymorph of hydroboracite remains stable up to ~14.4 GPa. Between 14.40(5) and 14.50(5) GPa, hydroboracite undergoes a phase transition. The space group of hydroboracite-II, which is metrically monoclinic, remains unclear due to the sharp decrease in the number of observed reflections. A similar response to pressure-induced phase transitions has been reported for other hydrous borates (*e.g.*, inyoite, inderborite; Comboni et al. 2022a, 2024);

(2) The elastic parameters of hydroboracite have been determined, and the elastic behaviour has been described in detail. Hydroboracite is a soft, anisotropic borate that compresses mainly

on the *bc* plane. These data will contribute to improving the thermodynamic database of hydrous borates;

(3) With increasing pressure, similarly to all the hydrous borate structure previously studied (*e.g.*, kurnakovite, colemanite; Lotti et al. 2017; Pagliaro et al. 2021), the bulk moduli of the Ca-, Mg- and B-coordination polyhedra are significantly larger than the bulk compressibility. Pressure is accommodated primarily by deformation of the hydrogen-bond network and by tilting of the Ca-, Mg-, and B-polyhedra around bridging oxygen sites.

(4) The hydroboracite-to-hydroboracite-II phase transition occurs at 14.45±0.2 GPa, consistent with values observed for other hydrous borates characterized by infinite $B\varphi_x$ units (*i.e.*, kernite, probertite, colemanite, jadarite; Lotti et al. 2017; Comboni et al. 2020a, 2022b). This finding strengthens the presumed correlation between the pressure at which the phase transition occurs and the total H_2O content (in wt.%, Figure 6).

(5) The bulk modulus of hydroboracite (K_{V0} = 41(1) GPa) is similar to the that of quartz (~37 GPa) and lower than those of other aggregates used in radiation shielding concretes (*e.g.*, colemanite K_{V0} = 67(4); Okuno 2005; Lotti et al. 2017).

Like colemanite, inderite, and inderborite, hydroboracite is a Na-free borate and therefore cannot promote ASR reactions (*i.e.,* alkali-silica reactions; Thomas 2011; Figueira et al. 2019; Mohammadi et al. 2020), which are known to undermine the durability of Portland cements. Considering its stability field at non-ambient conditions ((Valdez and Flores 2010), and this study) and its elastic parameters, hydroboracite has a potential to be utilised as a B-rich aggregate in radiation-shielding materials.

Acknowledgments

Three anonymous reviewers are thanked for the valuable and fruitful comments that improved the manuscript quality. ESRF is thanked for the allocation of the beamtime (proposal MA-5916, doi: 10.15151/ESRF-ES 1334154239). GDG, DC, PL and TB acknowledge the University of Milan through the project “Piano di Sostegno alla Ricerca 2023”. The work was partly supported by the Italian Ministry for University and Research (MUR) through the project “Dipartimenti di Eccellenza 2023–2027”.

Data availability

Data will be available upon request

Author contribution statement

Davide Comboni: Data curation, Formal analysis, Project administration, Writing original draft
Paolo Lotti: Data Curation, Validation, Writing – review & editing
Lisa Chiappella: Validation, Visualization
Tommaso Battiston: Formal analysis, Investigation
Gaston Garbarino: Investigation
Paola Giura: Conceptualization, Resources
G. Diego Gatta: Conceptualization, Writing – review & editing

SUPPLEMENTARY MATERIAL

Table S1:Eevolution with pressure of bonds length (in Å) and angles (in °) in hydroboracite (first experiment).

-First datatset-

	Mg-O3	Mg-O2	Mg-O1	Ca-O6	Ca-O9	Ca-O7	Ca-O9	B1-O6	B1-O4
0.0001	2.023(2)	2.053(2)	2.2219(8)	2.354(2)	2.432(2)	2.426(2)	2.644(2)	1.442(3)	1.464(3)
0.32(5)	2.020(3)	2.048(4)	2.211(2)	2.353(3)	2.427(3)	2.418(3)	2.636(3)	1.427(4)	1.474(4)
0.66(5)	2.016(2)	2.047(3)	2.199(2)	2.346(2)	2.417(2)	2.420(2)	2.635(2)	1.432(3)	1.478(3)
0.93(5)	2.013(2)	2.044(3)	2.196(2)	2.342(2)	2.411(3)	2.416(2)	2.627(2)	1.433(3)	1.477(3)
1.28(5)	2.010(2)	2.040(3)	2.190(2)	2.337(2)	2.404(3)	2.413(2)	2.620(2)	1.431(3)	1.473(3)
1.95(5)	2.004(2)	2.043(3)	2.181(2)	2.330(2)	2.398(3)	2.404(2)	2.614(2)	1.431(3)	1.475(3)
2.13(5)	1.999(2)	2.048(3)	2.179(2)	2.327(2)	2.389(2)	2.400(2)	2.611(2)	1.437(3)	1.473(3)
2.90(5)	1.993(2)	2.043(3)	2.166(2)	2.322(2)	2.376(2)	2.394(2)	2.602(2)	1.428(3)	1.474(3)
3.68(5)	1.988(2)	2.046(4)	2.154(2)	2.311(3)	2.365(3)	2.383(2)	2.590(2)	1.429(4)	1.475(5)
4.12(5)	1.984(2)	2.039(4)	2.148(2)	2.304(3)	2.361(3)	2.377(2)	2.586(2)	1.428(4)	1.465(5)
4.94(5)	1.983(3)	2.054(4)	2.149(2)	2.306(3)	2.361(3)	2.379(3)	2.591(3)	1.431(4)	1.472(6)
5.42(5)	1.974(2)	2.038(4)	2.132(2)	2.291(3)	2.347(3)	2.367(3)	2.573(3)	1.419(4)	1.466(6)
6.02(5)	1.971(2)	2.035(4)	2.127(2)	2.291(3)	2.338(3)	2.363(2)	2.565(2)	1.425(4)	1.470(4)
6.76(5)	1.964(2)	2.041(4)	2.120(2)	2.282(3)	2.326(3)	2.356(2)	2.557(2)	1.427(4)	1.473(4)
7.35(5)	1.958(2)	2.038(4)	2.112(2)	2.273(3)	2.323(3)	2.356(3)	2.553(2)	1.429(4)	1.472(4)
8.05(5)	1.957(2)	2.037(4)	2.106(2)	2.270(3)	2.320(3)	2.348(2)	2.548(2)	1.431(4)	1.467(4)
8.92(5)	1.958(2)	2.039(4)	2.101(2)	2.262(3)	2.309(3)	2.339(3)	2.540(2)	1.421(4)	1.471(4)
9.50(5)	1.954(2)	2.031(4)	2.090(2)	2.256(3)	2.303(3)	2.334(3)	2.538(2)	1.433(4)	1.464(4)
10.66(5)	1.953(2)	2.038(4)	2.088(2)	2.249(3)	2.296(3)	2.323(3)	2.533(2)	1.420(4)	1.472(4)
11.36(5)	1.943(2)	2.033(4)	2.079(2)	2.241(3)	2.286(3)	2.316(2)	2.524(2)	1.420(4)	1.465(3)
11.75(5)	1.942(2)	2.035(4)	2.077(2)	2.240(3)	2.284(3)	2.313(2)	2.522(2)	1.421(4)	1.466(3)
12.22(5)	1.938(2)	2.033(4)	2.072(2)	2.231(3)	2.280(3)	2.315(3)	2.518(3)	1.422(4)	1.467(4)
12.99(5)	1.938(2)	2.035(5)	2.066(3)	2.226(3)	2.276(4)	2.309(3)	2.512(3)	1.420(4)	1.470(4)
13.38(5)	1.932(2)	2.030(5)	2.067(3)	2.227(3)	2.272(3)	2.304(3)	2.509(3)	1.417(5)	1.454(7)
14.40(5)	1.931(4)	2.023(5)	2.059(3)	2.215(4)	2.257(4)	2.294(4)	2.502(3)	1.404(6)	1.467(9)

-First datatset-

	B1-O3	**B1-O5**	**B2-O8**	**B2-O6**	**B2-O9**	**B2-O7**	**B3-O7**	**B3-O4**	**B3-O5**
0.0001	1.495(3)	1.506(3)	1.467(3)	1.459(4)	1.471(4)	1.506(3)	1.369(4)	1.368(3)	1.375(4)
0.32(5)	1.492(6)	1.496(5)	1.459(6)	1.476(4)	1.472(4)	1.510(5)	1.358(5)	1.368(6)	1.384(4)
0.66(5)	1.489(5)	1.496(4)	1.454(5)	1.470(3)	1.480(3)	1.498(4)	1.365(4)	1.366(4)	1.378(3)
0.93(5)	1.484(5)	1.497(4)	1.452(5)	1.471(3)	1.473(4)	1.499(4)	1.362(4)	1.368(4)	1.378(3)
1.28(5)	1.480(5)	1.493(4)	1.449(5)	1.467(3)	1.472(4)	1.495(4)	1.360(4)	1.365(4)	1.375(3)
1.95(5)	1.475(5)	1.496(4)	1.452(5)	1.470(4)	1.471(3)	1.501(4)	1.362(4)	1.367(4)	1.376(4)
2.13(5)	1.477(5)	1.501(4)	1.449(4)	1.469(3)	1.470(3)	1.498(4)	1.362(4)	1.370(3)	1.371(4)
2.90(5)	1.479(5)	1.499(4)	1.449(4)	1.470(3)	1.469(3)	1.495(4)	1.359(4)	1.368(4)	1.373(4)
3.68(5)	1.475(4)	1.494(5)	1.455(5)	1.468(3)	1.468(4)	1.492(4)	1.360(5)	1.372(5)	1.367(4)
4.12(5)	1.472(4)	1.500(5)	1.442(5)	1.468(3)	1.472(4)	1.499(4)	1.358(5)	1.370(5)	1.372(4)
4.94(5)	1.481(4)	1.510(5)	1.455(6)	1.473(3)	1.474(4)	1.496(5)	1.358(5)	1.378(6)	1.371(4)
5.42(5)	1.474(4)	1.502(5)	1.446(6)	1.468(3)	1.469(4)	1.494(5)	1.357(5)	1.361(6)	1.371(4)
6.02(5)	1.465(5)	1.503(5)	1.447(5)	1.468(3)	1.465(4)	1.498(4)	1.354(5)	1.362(5)	1.366(4)
6.76(5)	1.464(5)	1.495(5)	1.439(6)	1.466(3)	1.467(4)	1.492(5)	1.356(5)	1.365(5)	1.365(4)
7.35(5)	1.461(6)	1.502(5)	1.442(6)	1.461(3)	1.467(4)	1.484(5)	1.351(5)	1.367(6)	1.365(4)
8.05(5)	1.460(6)	1.491(5)	1.438(5)	1.462(3)	1.466(4)	1.486(4)	1.356(5)	1.363(5)	1.363(4)
8.92(5)	1.447(6)	1.502(5)	1.436(6)	1.466(3)	1.463(4)	1.489(5)	1.358(5)	1.356(6)	1.366(4)
9.50(5)	1.446(6)	1.496(5)	1.433(6)	1.460(4)	1.457(4)	1.490(5)	1.349(5)	1.362(6)	1.365(4)
10.66(5)	1.448(6)	1.507(5)	1.426(6)	1.464(3)	1.471(4)	1.490(5)	1.356(5)	1.362(6)	1.363(4)
11.36(5)	1.446(6)	1.504(5)	1.419(6)	1.462(3)	1.467(4)	1.492(5)	1.350(5)	1.364(5)	1.358(4)
11.75(5)	1.451(5)	1.500(5)	1.433(5)	1.464(3)	1.461(4)	1.482(4)	1.356(4)	1.359(5)	1.360(4)
12.22(5)	1.452(6)	1.495(6)	1.426(7)	1.461(4)	1.458(4)	1.488(5)	1.350(5)	1.351(6)	1.363(5)
12.99(5)	1.440(6)	1.492(6)	1.416(7)	1.458(4)	1.460(4)	1.481(6)	1.360(6)	1.349(7)	1.361(5)
13.38(5)	1.465(4)	1.490(6)	1.423(7)	1.458(4)	1.459(5)	1.482(6)	1.348(6)	1.352(7)	1.358(5)
14.40(5)	1.465(5)	1.472(7)	1.429(9)	1.458(5)	1.461(7)	1.478(7)	1.345(8)	1.347(9)	1.355(6)

Mgφ_6 polyhedra, First datatset-

***P* (GPa)**	**Avg bond length (Å)**	**Polyhedral volume (Å^3)**	**Distortion index**	**Quadratic elongation**	**Bond angle variance (deg^2)**
0.0001	2.099	12.27	0.039	1.005	6.87
0.32(5)	2.093	12.17	0.038	1.005	4.96
0.66(5)	2.087	12.08	0.036	1.004	3.46
0.93(5)	2.084	12.03	0.036	1.004	3.46
1.28(5)	2.080	11.96	0.035	1.004	3.43
1.95(5)	2.076	11.90	0.034	1.003	2.29
2.13(5)	2.075	11.88	0.033	1.003	2.15
2.90(5)	2.067	11.75	0.032	1.003	1.38
3.68(5)	2.063	11.68	0.030	1.003	1.22
4.12(5)	2.057	11.58	0.029	1.003	1.09
4.94(5)	2.062	11.66	0.028	1.003	1.07
5.42(5)	2.048	11.43	0.027	1.002	1.28
6.02(5)	2.044	11.37	0.027	1.002	1.69
6.76(5)	2.042	11.32	0.025	1.003	2.32
7.35(5)	2.036	11.22	0.025	1.003	2.65
8.05(5)	2.033	11.18	0.025	1.003	3.47
8.92(5)	2.033	11.17	0.025	1.003	3.90
9.50(5)	2.025	11.05	0.023	1.003	4.26
10.66(5)	2.026	11.05	0.024	1.003	6.06
11.36(5)	2.018	10.91	0.025	1.004	7.03
11.75(5)	2.018	10.91	0.025	1.004	8.06
12.22(5)	2.014	10.84	0.025	1.004	8.63
12.99(5)	2.013	10.83	0.025	1.004	9.19
13.38(5)	2.010	10.76	0.026	1.005	10.54
14.40(5)	2.004	10.67	0.024	1.005	11.63

Caφ_8 -First datatset-

P **(GPa)**	**Avg bond length (Å)**	**Polyhedral volume (Å^3)**	**Distortion index**	**Quadratic elongation**
0.0001	2.464	24.88	0.037	7.43
0.32(5)	2.459	24.78	0.036	7.45
0.66(5)	2.454	24.68	0.037	7.43
0.93(5)	2.449	24.53	0.036	7.44
1.28(5)	2.444	24.37	0.036	7.44
1.95(5)	2.437	24.24	0.036	7.44
2.13(5)	2.432	24.10	0.037	7.43
2.90(5)	2.423	23.91	0.037	7.44
3.68(5)	2.412	23.63	0.037	7.44
4.12(5)	2.407	23.51	0.037	7.43
4.94(5)	2.409	23.61	0.038	7.41
5.42(5)	2.395	23.23	0.037	7.42
6.02(5)	2.389	23.10	0.037	7.45
6.76(5)	2.380	22.88	0.037	7.43
7.35(5)	2.376	22.78	0.037	7.42
8.05(5)	2.371	22.68	0.037	7.42
8.92(5)	2.362	22.45	0.038	7.42
9.50(5)	2.358	22.33	0.038	7.40
10.66(5)	2.350	22.19	0.039	7.39
11.36(5)	2.342	21.97	0.039	7.38
11.75(5)	2.340	21.93	0.039	7.38
12.22(5)	2.336	21.82	0.039	7.36
12.99(5)	2.331	21.72	0.039	7.37
13.38(5)	2.328	21.66	0.039	7.38
14.40(5)	2.317	21.39	0.040	7.35

-First dataset -

P **(GPa)**	**O7–$\widehat{\mathrm{O6}}$–O7**	**Mg–$\widehat{\mathrm{O1}}$–Mg**	**O1···O4**	**O2–$\widehat{\mathrm{O1}}$–O2**	**O2–$\widehat{\mathrm{O5}}$–O3**	**O2···O5**
0.0001	108.91(7)	135.96(9)	2.684(2)	58.72(7)	120.86(11)	2.715(3)
0.32(5)	108.45(16)	136.4(3)	2.680(4)	58.58(13)	121.10(13)	2.720(5)
0.66(5)	108.13(12)	137.0(2)	2.675(3)	58.73(10)	121.25(11)	2.713(4)
0.93(5)	107.84(13)	136.5(2)	2.664(3)	58.35(10)	121.36(11)	2.711(4)
1.28(5)	107.81(13)	136.4(2)	2.660(3)	58.35(10)	121.34(11)	2.706(4)
1.95(5)	106.77(13)	136.1(2)	2.639(3)	57.68(10)	121.49(11)	2.700(4)
2.13(5)	106.51(12)	135.8(2)	2.635(3)	57.28(10)	121.27(11)	2.692(4)
2.90(5)	105.91(12)	135.8(2)	2.625(3)	57.05(10)	121.63(11)	2.687(4)
3.68(5)	105.26(14)	135.7(2)	2.609(4)	56.72(11)	121.67(12)	2.677(4)
4.12(5)	105.00(14)	135.6(2)	2.602(3)	56.58(11)	121.86(12)	2.679(4)
4.94(5)	104.57(15)	135.5(3)	2.597(4)	56.17(12)	122.02(14)	2.669(4)
5.42(5)	104.24(15)	135.3(3)	2.587(4)	56.02(13)	122.21(14)	2.665(5)
6.02(5)	103.51(13)	134.9(2)	2.579(3)	55.86(11)	122.21(12)	2.657(4)
6.76(5)	103.20(14)	134.7(2)	2.566(3)	55.38(11)	122.30(12)	2.653(4)
7.35(5)	102.90(15)	134.7(3)	2.560(4)	55.38(12)	122.47(14)	2.640(5)
8.05(5)	102.44(14)	134.3(2)	2.550(3)	55.05(11)	122.67(13)	2.642(4)
8.92(5)	101.94(14)	133.8(3)	2.540(4)	54.68(12)	122.91(13)	2.629(4)
9.50(5)	101.79(15)	134.3(3)	2.537(4)	54.80(13)	123.15(14)	2.634(5)
10.66(5)	101.25(14)	133.7(3)	2.528(3)	54.35(12)	123.32(14)	2.620(4)
11.36(5)	101.01(14)	133.5(3)	2.521(3)	54.27(12)	123.33(13)	2.613(4)
11.75(5)	100.71(13)	133.2(2)	2.516(3)	54.19(11)	123.58(12)	2.604(4)
12.22(5)	100.65(16)	133.2(3)	2.510(4)	53.99(13)	123.76(15)	2.604(5)
12.99(5)	100.28(17)	132.9(3)	2.504(4)	53.83(14)	123.98(16)	2.600(5)
13.38(5)	100.06(17)	132.5(3)	2.500(4)	53.71(14)	123.96(16)	2.598(5)
14.40(5)	100.0(2)	132.3(4)	2.490(5)	53.60(17)	124.1(2)	2.594(6)

-

Table S2: Evolution with pressure of bonds length (in Å) and angles (in °) and other geometrical parameters in hydroboracite (second experiment).

-Second datatset-									
***P* (GPa)**	**Mg-O3**	**Mg-O2**	**Mg-O1**	**Ca-O6**	**Ca-O9**	**Ca-O7**	**Ca-O9**	**B1-O6**	**B1-O4**
0.0001	2.024(2)	2.052(2)	2.2227(8)	2.352(2)	2.431(2)	2.427(2)	2.644(2)	1.444(3)	1.467(3)
0.54(5)	2.010(9)	2.059(3)	2.211(1)	2.327(6)	2.425(3)	2.414(8)	2.632(4)	1.44(2)	1.469(10)
0.87(5)	2.002(7)	2.057(2)	2.205(1)	2.335(5)	2.412(2)	2.414(6)	2.631(3)	1.42(1)	1.473(7)
1.22(5)	1.995(7)	2.055(2)	2.197(1)	2.335(5)	2.406(2)	2.409(6)	2.623(3)	1.41(1)	1.473(7)
1.76(5)	2.006(7)	2.053(2)	2.187(1)	2.330(5)	2.397(2)	2.402(6)	2.617(3)	1.42(1)	1.472(7)
2.21(5)	1.999(7)	2.052(3)	2.179(1)	2.327(5)	2.388(3)	2.394(7)	2.609(3)	1.42(1)	1.469(8)
2.95(5)	1.990(7)	2.052(2)	2.169(1)	2.314(5)	2.378(3)	2.391(6)	2.600(4)	1.42(1)	1.472(7)
3.47(5)	1.983(7)	2.052(2)	2.161(1)	2.309(5)	2.368(3)	2.379(6)	2.593(4)	1.43(1)	1.470(7)
4.17(5)	1.987(8)	2.052(3)	2.155(1)	2.310(5)	2.358(3)	2.370(7)	2.587(4)	1.44(1)	1.463(8)
4.69(5)	1.981(7)	2.054(2)	2.155(1)	2.306(5)	2.361(2)	2.370(6)	2.589(3)	1.43(1)	1.472(7)
5.14(5)	1.979(7)	2.052(2)	2.142(1)	2.300(5)	2.346(2)	2.359(6)	2.576(3)	1.43(1)	1.465(7)
5.87(5)	1.979(8)	2.051(3)	2.134(1)	2.294(5)	2.339(3)	2.351(7)	2.570(4)	1.42(1)	1.466(8)
6.41(5)	1.970(7)	2.048(3)	2.128(1)	2.292(5)	2.331(3)	2.349(6)	2.564(4)	1.42(1)	1.466(7)
6.87(5)	1.969(7)	2.047(2)	2.122(1)	2.285(5)	2.323(2)	2.343(6)	2.560(3)	1.43(1)	1.463(7)
7.55(5)	1.963(7)	2.046(3)	2.117(1)	2.281(5)	2.319(3)	2.340(6)	2.555(4)	1.41(1)	1.464(7)
8.65(5)	1.958(8)	2.054(3)	2.119(1)	2.279(5)	2.319(3)	2.336(7)	2.558(4)	1.41(1)	1.474(8)
9.06(5)	1.950(9)	2.043(3)	2.103(1)	2.254(6)	2.305(3)	2.325(7)	2.541(4)	1.41(2)	1.467(9)
9.98(5)	1.955(8)	2.042(3)	2.095(1)	2.264(5)	2.295(3)	2.318(7)	2.536(4)	1.40(1)	1.464(8)
10.59(5)	1.954(8)	2.046(3)	2.090(1)	2.254(5)	2.289(3)	2.315(7)	2.529(4)	1.42(2)	1.459(9)
11.30(5)	1.948(8)	2.043(3)	2.085(1)	2.241(5)	2.285(3)	2.308(7)	2.525(4)	1.42(2)	1.456(9)
11.86(5)	1.947(8)	2.040(3)	2.081(1)	2.242(5)	2.280(3)	2.305(7)	2.520(4)	1.42(1)	1.459(8)
12.55(5)	1.944(9)	2.039(3)	2.077(1)	2.244(6)	2.276(3)	2.299(8)	2.514(4)	1.39(2)	1.463(9)
13.17(5)	1.94(1)	2.044(4)	2.079(2)	2.242(7)	2.275(4)	2.30(1)	2.515(6)	1.41(2)	1.47(1)
14.08(5)	1.94(2)	2.050(8)	2.071(3)	2.25(1)	2.254(8)	2.295(2)	2.505(10)	1.40(3)	1.466(12)

-Second datatset-

***P* (GPa)**	**B1-O3**	**B1-O5**	**B2-O8**	**B2-O6**	**B2-O9**	**B2-O7**	**B3-O7**	**B3-O5**	**B3-O4**
0.0001	1.494(3)	1.502(3)	1.469(3)	1.459(3)	1.471(3)	1.504(3)	1.368(3)	1.376(3)	1.368(3)
0.54(5)	1.495(8)	1.514(7)	1.459(5)	1.466(10)	1.49(2)	1.493(7)	1.36(1)	1.38(1)	1.382(6)
0.87(5)	1.500(6)	1.515(5)	1.466(4)	1.466(8)	1.47(1)	1.500(5)	1.36(1)	1.372(4)	1.376(9)
1.22(5)	1.494(6)	1.513(5)	1.464(4)	1.469(8)	1.46(1)	1.498(5)	1.35(1)	1.374(10)	1.374(5)
1.76(5)	1.480(6)	1.511(5)	1.461(4)	1.463(8)	1.46(1)	1.494(5)	1.36(1)	1.369(4)	1.374(10)
2.21(5)	1.479(6)	1.507(5)	1.460(4)	1.468(8)	1.44(1)	1.498(6)	1.36(1)	1.37(1)	1.365(5)
2.95(5)	1.480(6)	1.508(5)	1.460(4)	1.467(8)	1.45(1)	1.496(6)	1.35(1)	1.372(10)	1.366(4)
3.47(5)	1.473(6)	1.496(5)	1.458(4)	1.466(8)	1.43(1)	1.499(6)	1.36(1)	1.365(10)	1.359(4)
4.17(5)	1.462(7)	1.489(5)	1.448(5)	1.470(9)	1.44(1)	1.495(6)	1.36(1)	1.36(1)	1.366(5)
4.69(5)	1.469(6)	1.501(5)	1.455(4)	1.475(8)	1.46(1)	1.496(5)	1.36(1)	1.371(9)	1.372(4)
5.14(5)	1.460(6)	1.491(5)	1.449(4)	1.472(8)	1.45(1)	1.494(5)	1.35(1)	1.371(9)	1.369(4)
5.87(5)	1.462(7)	1.494(6)	1.443(5)	1.466(9)	1.45(2)	1.496(6)	1.36(1)	1.37(1)	1.368(5)
6.41(5)	1.463(6)	1.495(5)	1.441(4)	1.466(8)	1.45(1)	1.491(6)	1.35(1)	1.374(9)	1.370(4)
6.87(5)	1.457(5)	1.490(5)	1.44(1)	1.470(8)	1.445(4)	1.495(5)	1.34(1)	1.373(9)	1.372(4)
7.55(5)	1.462(6)	1.496(5)	1.441(4)	1.467(8)	1.45(1)	1.492(6)	1.34(1)	1.374(10)	1.368(4)
8.65(5)	1.469(7)	1.504(5)	1.444(4)	1.471(9)	1.45(1)	1.505(6)	1.34(1)	1.380(10)	1.379(4)
9.06(5)	1.464(7)	1.503(6)	1.436(5)	1.456(10)	1.47(2)	1.491(7)	1.34(1)	1.37(1)	1.375(5)
9.98(5)	1.456(7)	1.498(5)	1.434(5)	1.465(9)	1.44(1)	1.489(6)	1.34(1)	1.371(5)	1.37(1)
10.59(5)	1.451(7)	1.492(6)	1.438(5)	1.464(9)	1.44(1)	1.498(6)	1.33(1)	1.37(1)	1.375(5)
11.30(5)	1.455(7)	1.492(6)	1.430(5)	1.462(9)	1.45(1)	1.490(6)	1.34(1)	1.37(1)	1.374(5)
11.86(5)	1.449(7)	1.490(5)	1.430(4)	1.462(9)	1.45(1)	1.491(6)	1.33(1)	1.37(1)	1.372(5)
12.55(5)	1.453(7)	1.493(6)	1.426(5)	1.463(10)	1.44(2)	1.490(7)	1.33(1)	1.37(1)	1.376(5)
13.17(5)	1.449(9)	1.496(8)	1.428(6)	1.46(1)	1.43(2)	1.503(9)	1.33(2)	1.36(2)	1.375(7)
14.08(5)	1.43(2)	1.47(2)	1.425(7)	1.463(13)	1.42(3)	1.500(9)	1.33(2)	1.36(2)	1.372(7)

Mgφ_6 -Second datatset-

P(GPa)	Avg bond length (Å)	Polyhedral volume (Å^3)	Distortion index	Quadratic elongation	Bond angle variance (deg^2)
0.0001	2.100	12.27	0.039	1.005	7.12
0.54(5)	2.093	12.17	0.038	1.005	5.93
0.87(5)	2.088	12.09	0.037	1.005	5.18
1.22(5)	2.082	11.99	0.037	1.005	4.54
1.76(5)	2.082	11.99	0.034	1.004	3.41
2.21(5)	2.077	11.91	0.033	1.003	2.70
2.95(5)	2.070	11.80	0.032	1.003	2.25
3.47(5)	2.065	11.72	0.031	1.003	1.97
4.17(5)	2.065	11.70	0.029	1.003	2.09
4.69(5)	2.063	11.68	0.030	1.003	2.01
5.14(5)	2.058	11.59	0.027	1.003	2.11
5.87(5)	2.055	11.54	0.026	1.003	2.45
6.41(5)	2.049	11.44	0.026	1.003	2.63
6.87(5)	2.046	11.40	0.025	1.003	2.95
7.55(5)	2.042	11.32	0.026	1.003	3.37
8.65(5)	2.044	11.35	0.028	1.003	4.20
9.06(5)	2.032	11.15	0.027	1.003	5.26
9.98(5)	2.031	11.13	0.025	1.003	5.61
10.59(5)	2.030	11.10	0.025	1.003	6.72
11.30(5)	2.025	11.03	0.026	1.004	7.89
11.86(5)	2.023	10.98	0.025	1.004	8.34
12.55(5)	2.020	10.93	0.025	1.004	9.04
13.17(5)	2.022	10.96	0.026	1.004	10.04
14.08(5)	2.018	10.89	0.026	1.005	10.40

Caφ_8 -Second datatset-

P **(GPa)**	**Avg bond length (Å)**	**Polyhedral volume (Å^3)**	**Distortion index**	**Quadratic elongation**
0.0001	2.463	24.85	0.037	7.42
0.54(5)	2.450	24.58	0.037	7.36
0.87(5)	2.448	24.51	0.037	7.40
1.22(5)	2.443	24.38	0.037	7.42
1.76(5)	2.436	24.18	0.037	7.42
2.21(5)	2.430	23.99	0.037	7.44
2.95(5)	2.421	23.79	0.037	7.42
3.47(5)	2.412	23.54	0.037	7.42
4.17(5)	2.406	23.42	0.038	7.44
4.69(5)	2.407	23.55	0.038	7.42
5.14(5)	2.396	23.21	0.038	7.44
5.87(5)	2.389	23.05	0.038	7.43
6.41(5)	2.384	22.93	0.038	7.45
6.87(5)	2.378	22.79	0.038	7.43
7.55(5)	2.374	22.71	0.038	7.43
8.65(5)	2.373	22.73	0.039	7.41
9.06(5)	2.356	22.32	0.039	7.38
9.98(5)	2.354	22.23	0.039	7.43
10.59(5)	2.347	22.09	0.039	7.41
11.30(5)	2.340	21.91	0.040	7.38
11.86(5)	2.337	21.85	0.039	7.40
12.55(5)	2.333	21.76	0.039	7.42
13.17(5)	2.334	21.78	0.039	7.41
14.08(5)	2.329	21.63	0.039	7.41

Mgφ_6 -Second datatset-

P **(GPa)**	**O7– $\widehat{\mathrm{O6}}$ –O7**	**Mg–$\widehat{\mathrm{O1}}$–Mg**	**O1···O4**	**O2–$\widehat{\mathrm{O1}}$–O2**	**O2– $\widehat{\mathrm{O5}}$ –O3**	**O2···O5**
0.0001	108.94(7)	135.89(9)	2.683(2)	58.73(7)	120.84(10)	2.714(3)
0.54(5)	108.14(13)	135.52(17)	2.665(8)	57.87(16)	121.1(3)	2.691(9)
0.87(5)	107.90(10)	135.46(12)	2.655(6)	57.60(12)	121.0(3)	2.694(7)
1.22(5)	107.46(10)	135.48(12)	2.648(6)	57.39(12)	120.9(3)	2.690(7)
1.76(5)	107.01(10)	135.47(12)	2.644(6)	57.19(13)	121.3(3)	2.685(7)
2.21(5)	106.53(10)	135.36(12)	2.640(6)	56.92(12)	121.4(3)	2.681(7)
2.95(5)	105.85(10)	135.11(13)	2.623(6)	56.56(13)	121.5(3)	2.671(7)
3.47(5)	105.43(10)	134.99(13)	2.620(6)	56.35(13)	121.4(3)	2.668(7)
4.17(5)	104.89(11)	134.60(14)	2.602(7)	55.75(14)	121.7(3)	2.667(8)
4.69(5)	104.58(10)	134.55(12)	2.594(6)	55.61(13)	121.9(3)	2.666(7)
5.14(5)	104.25(10)	134.38(12)	2.585(6)	55.40(13)	121.9(3)	2.654(7)
5.87(5)	103.80(12)	134.10(14)	2.575(7)	55.24(15)	122.4(3)	2.645(8)
6.41(5)	103.47(10)	134.00(13)	2.564(6)	54.99(14)	122.3(3)	2.645(7)
6.87(5)	103.19(10)	133.88(12)	2.558(6)	54.91(13)	122.4(3)	2.640(7)
7.55(5)	102.83(10)	133.70(13)	2.555(6)	54.60(14)	122.7(3)	2.636(7)
8.65(5)	102.35(11)	133.38(14)	2.546(7)	54.31(15)	122.7(3)	2.637(8)
9.06(5)	101.942(131)	133.15(16)	2.528(7)	54.2(3)	123.2(3)	2.621(9)
9.98(5)	101.80(11)	133.06(15)	2.520(7)	53.82(15)	123.2(3)	2.620(8)
10.59(5)	101.35(12)	132.87(15)	2.519(7)	53.86(16)	123.5(3)	2.607(8)
11.30(5)	101.12(12)	132.57(15)	2.511(7)	53.71(17)	123.7(3)	2.600(8)
11.86(5)	100.93(12)	132.47(15)	2.503(7)	53.53(16)	123.8(3)	2.600(8)
12.55(5)	100.67(13)	132.20(16)	2.491(7)	53.20(18)	123.9(3)	2.600(9)
13.17(5)	100.35(17)	131.9(2)	2.491(9)	53.1(2)	123.9(4)	2.596(11)
14.08(5)	100.3(2)	131.8(2)	2.485(10)	53.0(6)	124.0(5)	2.59(1)

Figure S1: Evolution of the Eulerian finite strain (*fe*) *vs*. the normalised pressure (*F*) of hydroboracite. The non-horizontal linear trend of the data points confirm that a third-order BM-EoS is appropriate to model the compressional *P*-*V* behaviour.

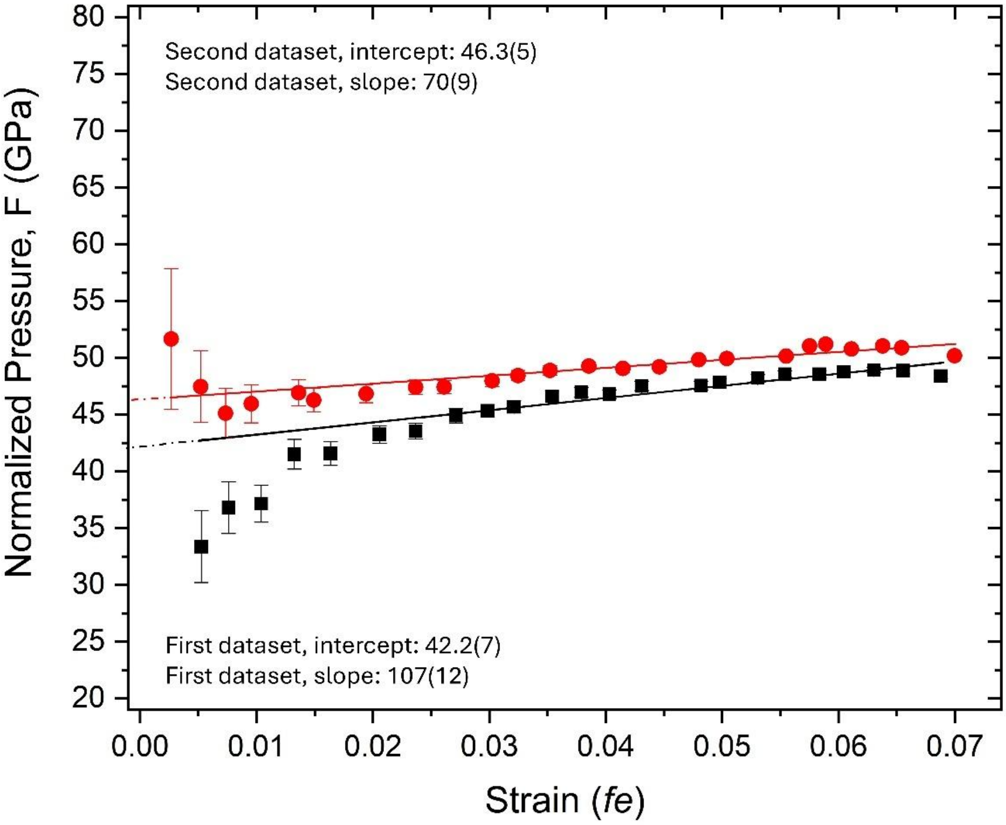

REFERENCES

Angel RJ (2011) Win_Strain. A program to calculate strain tensors from unit-cell parameters. http://www.rossangel.com/home.htm.

Angel RJ, Alvaro M, Gonzalez-Platas J (2014) EosFit7c and a Fortran module (library) for equation of state calculations. Zeitschrift fur Krist 229:405–419. https://doi.org/10.1515/zkri-2013-1711

Rumanov IM, Ashirov A (1962) The crystal structure of hydroboracite $CaMg[B_3O_4(OH)_3]_2 \cdot 3H_2O$. Soviet physics- Crystallography 8, 6, 665-680

Baur WH (1974) The geometry of polyhedral distortions. Predictive relationships for the phosphate group. Acta Crystallogr Sect B Struct Crystallogr Cryst Chem 30:1195–1215. https://doi.org/10.1107/s0567740874004560

Bekker TB, Podborodnikov I V., Sagatov NE, et al (2022) γ-BaB_2O_4: High-Pressure High-Temperature Polymorph of Barium Borate with Edge-Sharing BO_4 Tetrahedra. Inorg Chem 61:2340–2350. https://doi.org/10.1021/acs.inorgchem.1c03760

Birch F (1947) Finite elastic strain of cubic crystals. Phys Rev 71:809–824. https://doi.org/10.1103/PhysRev.71.809

Blengini GA, Latunussa CEL, Eynard U, et al (2020) Study on the EU's list of Critical Raw Materials (2020) Final Report

Carter RS, Palevsky H, Myers VW, Hughes DJ (1953) Thermal neutron absorption cross sections of boron and gold. Phys Rev 92:716–721. https://doi.org/10.1103/PhysRev.92.716

Christ CL, Clark JR, Evans HT (1954) The structure of colemanite, $CaB_3O_4(OH)_3 \cdot H_2O$, determined by the direct method of Hauptman & Karle. Acta Crystallogr 7:453–454. https://doi.org/10.1107/S0365110X54001375

Comboni D, Battiston T, Lotti P, et al (2024) Atomic-scale deformation mechanisms at high-pressure in inderborite, $CaMg[B_3O_3(OH)_5]_2 (H_2O)_4 \cdot 2H_2O$. Mineral Mag 3:1–34. https://doi.org/10.1180/mgm.2024.29

Comboni D, Battiston T, Pagliaro F, et al (2022a) High-pressure behaviour and atomic-scale deformation mechanisms in inyoite, $CaB_3O_3(OH)_5 \cdot 4H_2O$. Phys Chem Miner 49:1–10. https://doi.org/10.1007/s00269-021-01173-3

Comboni D, Battiston T, Rumsey MS, et al (2022b) High-pressure behavior and phase transition of jadarite, a promising B and Li mineral commodity. J Am Ceram Soc 7011–7021. https://doi.org/10.1111/jace.18659

Comboni D, Pagliaro F, Gatta GD, et al (2020a) High-pressure behavior and phase stability of $Na_2B_4O_6(OH)_2 \cdot 3H_2O$ (kernite). J Am Ceram Soc 103:5291–5301. https://doi.org/10.1111/jace.17185

Comboni D, Pagliaro F, Gatta GD, et al (2020b) High-pressure behaviour and phase stability of $Ca_2B_6O_6(OH)_{10} \cdot 2(H_2O)$(meyerhofferite). Phys Chem Miner 47. https://doi.org/10.1007/s00269-020-01117-3

Comboni D, Pagliaro F, Gatta GD, et al (2021) Phase transition and high-pressure behavior of ulexite, a potential aggregate in radiation-shielding concretes. Constr Build Mater 291:123188. https://doi.org/10.1016/j.conbuildmat.2021.123188

Comboni D, Poreba T, Battiston T, et al (2023) On the anomalous high-pressure phase transition of inderite, $MgB_3O_3(OH)_5 \cdot 5H_2O$. Solid State Sci 140:107187. https://doi.org/10.1016/j.solidstatesciences.2023.107187

Demircioglu A (2023) Boron minerals of Turkey: Hydroboracite. Bull Miner Res Explor 1973:80, 8

Ezechi EH, Isa MH, Kutty SR, Sapari NB (2011) Boron recovery, Application and economic significance: a review. https://doi.org/10.1109/NatPC.2011.6136374

Figueira RB, Sousa R, Coelho L, et al (2019) Alkali-silica reaction in concrete: Mechanisms, mitigation and test methods. Constr Build Mater 222:903–931. https://doi.org/10.1016/j.conbuildmat.2019.07.230

Fischer W, Lischke M (1981) Hydroboracit von Woffleben, eine vorläufige Fundbeschreibung. Fundgrube 28–29

Foshag W. (1924) Famous mineral localities: Furnace Creek, Death Valley, California. Am Mineral 9:8–10

Frost RL, Scholz R, López A, et al (2014) Infrared and Raman spectroscopic characterization of the borate mineral hydroboracite $CaMg[B_3O_4(OH)_3]_2 \cdot 3H_2O$ - Implications for the molecular structure. J Mol Struct 1059:20–26. https://doi.org/10.1016/j.molstruc.2013.11.012

Gatta GD, Vignola P, Lee Y (2011) Stability of $(Cs, K)Al_4Be_5B_{11}O_{28}$ (londonite) at high pressure and high temperature: A potential neutron absorber material. Phys Chem Miner 38:429–434. https://doi.org/10.1007/s00269-011-0416-5

Glinicki MA, Antolik A, Gawlicki M (2018) Evaluation of compatibility of neutron-shielding boron aggregates with Portland cement in mortar. Constr Build Mater 164:731–738. https://doi.org/10.1016/j.conbuildmat.2017.12.228

Gonzalez-Platas J, Alvaro M, Nestola F, Angel R (2016) EosFit7-GUI: A new graphical user interface for equation of state calculations, analyses and teaching. J Appl Crystallogr 49:1377–1382. https://doi.org/10.1107/S1600576716008050

Gorelova L, Pakhomova A, Aprilis G, et al (2022) Edge-sharing BO_4 tetrahedra and penta-coordinated silicon in the high-pressure modification of $NaBSi_3O_8$. Inorg Chem Front 9:1735–1742. https://doi.org/10.1039/d2qi00101b

Hanfland M (2016) Crystallography at high pressure using synchrotron radiation. 15:30–31, chrome-extension://efaidnbmnnnibpcajpcglclefindmkaj/https://www.esrf.fr/files/live/sites/www/files/events/conferences/2019/HP%20school/HANFLAND%20abstract.pdf

Helvaci C (2017) Borate deposits: An overview and future forecast with regard to mineral deposits. J Boron 2:59–70

Helvaci C, Alonso RN (2000) Borate Deposits of Turkey and Argentina; A Summary and Geological Comparison. Turkish J Earth Sci 9:1–27. https://dergipark.org.tr/en/pub/boron/article/302668

Huang Z, Wang S, Dewhurst RD, et al (2020) Boron: Its Role in Energy-Related Processes and Applications. Angew Chemie - Int Ed 59:8800–8816. https://doi.org/10.1002/anie.201911108

Klotz S, Chervin JC, Munsch P, Le Marchand G (2009) Hydrostatic limits of 11 pressure transmitting media. J Phys D Appl Phys 42, 7. https://doi.org/10.1088/0022-3727/42/7/075413

Lotti P, Gatta GD, Comboni D, et al (2017) High-pressure behavior and P-induced phase transition of $CaB_3O_4(OH)_3 \cdot H_2O$ (colemanite). J Am Ceram Soc 100:2209–2220. https://doi.org/10.1111/jace.14730

Lotti P, Gatta GD, Demitri N, et al (2018) Crystal chemistry and temperature behavior of the natural hydrous borate colemanite, a mineral commodity of boron. Phys Chem Miner 45:405-422. https://doi.org/10.1007/s00269-017-0929-7

Mao HK, Xu J, Bell PM (1986) Calibration of the ruby pressure gauge to 800 kbar under quasi-hydrostatic conditions. J Geophys Res 91:4673- 4676. https://doi.org/10.1029/JB091iB05p04673

Mohammadi A, Ghiasvand E, Nili M (2020) Relation between mechanical properties of concrete and alkali-silica reaction (ASR); a review. Constr Build Mater 258:119567. https://doi.org/10.1016/j.conbuildmat.2020.119567

Momma K, Izumi F (2008) VESTA: A three-dimensional visualization system for electronic and structural analysis. J Appl Crystallogr 41:653–658. https://doi.org/10.1107/S0021889808012016

Okuno K (2005) Neutron shielding material based on colemanite and epoxy resin. Radiat Prot Dosimetry 115:258–261. https://doi.org/10.1093/rpd/nci154

Okuno K, Kawai M, Yamada H (2009) Development of Novel Neutron Shielding Concrete. Nucl Technol 168:545–552. https://doi.org/10.13182/NT09-A9241

Pagliaro F, Lotti P, Battiston T, et al (2021) Thermal and compressional behavior of the natural borate kurnakovite, $MgB_3O_3(OH)_5 \cdot 5H_2O$. Constr Build Mater 266:121094. https://doi.org/10.1016/j.conbuildmat.2020.121094

Palmer M, Swihart G (1996) Boron isotope geochemistry: An overview. In: Anovitz L, Grew E (eds) Boron: Mineralogy, Petrology, and Geochemistry. Mineralogical Society of America, Washington, pp 709–744. https://doi.org/10.1515/9781501509223-015

Pekov IV, Abramov DV (1993) Boron deposit of the Inder and its minerals. World of Stones 1:23–30. Mindat.org Ref. ID: 15934195

Petrícek V, Dušek M, Palatinus L (2014) Crystallographic computing system JANA2006: General features. Zeitschrift fur Krist. 229:345–352. https://doi.org/10.1515/zkri-2014-1737

Poreba T, Comboni D, Mezouar M, et al (2022) Tracking of Structural Phase Transitions via Single Crystal X-ray Diffraction at Extreme Conditions: Advantages of Extremely Brilliant Source. J Phys Condens Matter 35. https://doi.org/10.1088/1361-648X/aca50b

Rigaku Oxford Diffraction (2019) CrysAlisPro Software system, version 1.171.40.67a

Robinson K, Gibbs G V, Ribbe PH (1971) Quadratic Elongation: A Quantitative Measure of Distortion in Coordination Polyhedra. Science (80-) 172:567–570. https://doi.org/10.1126/science.172.3983.567

Sabelli C, Stoppioni A (1978) Refinement of the crystal structure of hydroboracite. 16:75–80. AMCSD ID: 0005149

Thomas M (2011) The effect of supplementary cementing materials on alkali-silica reaction: A review. Cem Concr Res 41:1224–1231. https://doi.org/10.1016/j.cemconres.2010.11.003

Valdez SK, Flores HR (2010) Thermal propierties of hydroboracite. In: Chung MP (ed) Handbook of borates: chemistry, production and applications. Nova Science Publisher, inc, 400 OSER AVE, STE 1600, HAUPPAUGE, NY 11788-3635 USA, pp 461–468

Waleed KH. Sh. Al-Juheishy (2020) Effect Of Boron On Some Industrial Crops: A Review. Mesopotamia J Agric 48:134–145. ISSN (Online): 2224-9796